Special Issue: General stream

Systems Article

Autonomous, Long-Range, Sensor Emplacement Using Unmanned Aircraft Systems

Adam Plowcha[1], Justin Bradley[1], Jacob Hogberg[1], Thomas Ammon[2], Mark Nail[2], Brittany Duncan[1] and Carrick Detweiler[1]

[1]Department of Computer Science and Engineering, University of Nebraska-Lincoln, Lincoln, Nebraska 68588

[2]Department of Mechanical Engineering, University of Nebraska-Lincoln, Lincoln, Nebraska 68588

Abstract: Automated, in-ground sensor emplacement can significantly improve remote, terrestrial, data collection capabilities. Utilizing a multicopter, unmanned aircraft system (UAS) for this purpose allows sensor insertion with minimal disturbance to the target site or surrounding area. However, developing an emplacement mechanism for a small multicopter, autonomy to manage the target selection and implantation process, as well as long-range deployment are challenging to address. We have developed an autonomous, multicopter UAS that can implant subsurface sensor devices. We enhanced the UAS autopilot with autonomy for target and landing zone selection, as well as ensuring the sensor is implanted properly in the ground. The multicopter UAS, limited by onboard energy, can be carried by a transport aircraft to within 1 km of the desired sensor location site and deployed by a novel parachuting-canister system. Through a comprehensive set of field trials and testing, we assess the effectiveness of each subsystem. We evaluate our system on missions covering distances up to 25 km away in mountains 1 km above the takeoff location.

Keywords: aerial robotics, environmental monitoring, mechanisms, sensors, terrestrial robotics

1. Introduction

Unmanned Aerial Systems (UAS) have transformed the way that scientists are able to collect remote sensor data. Beyond collecting remote imaging data, multi-rotor UASs have been used to precisely deploy ground surface sensors [Schwarzbach et al., 2012, Corke et al., 2004], water sensors [Bradley et al., 2015], and measure atmospheric boundary layer conditions [Islam et al., 2019]. Scientists, however, often need to *emplace sensors in the ground* to monitor everything from soil moisture to earthquakes. In our prior work [Sun et al., 2018, Plowcha et al., 2018] we developed the first UAS capable of digging a hole in the ground and emplacing a sensor. However, UAS in this size class with current fuel/battery technology are severely limited in range and flight duration and hence do not

Received: 28 September 2020; revised: 29 April 2021; accepted: 24 May 2021; published: 30 March 2022.

Correspondence: Adam Plowcha, Department of Computer Science and Engineering, University of Nebraska-Lincoln, Lincoln, Nebraska 68588, Email: adam.plowcha@huskers.unl.edu

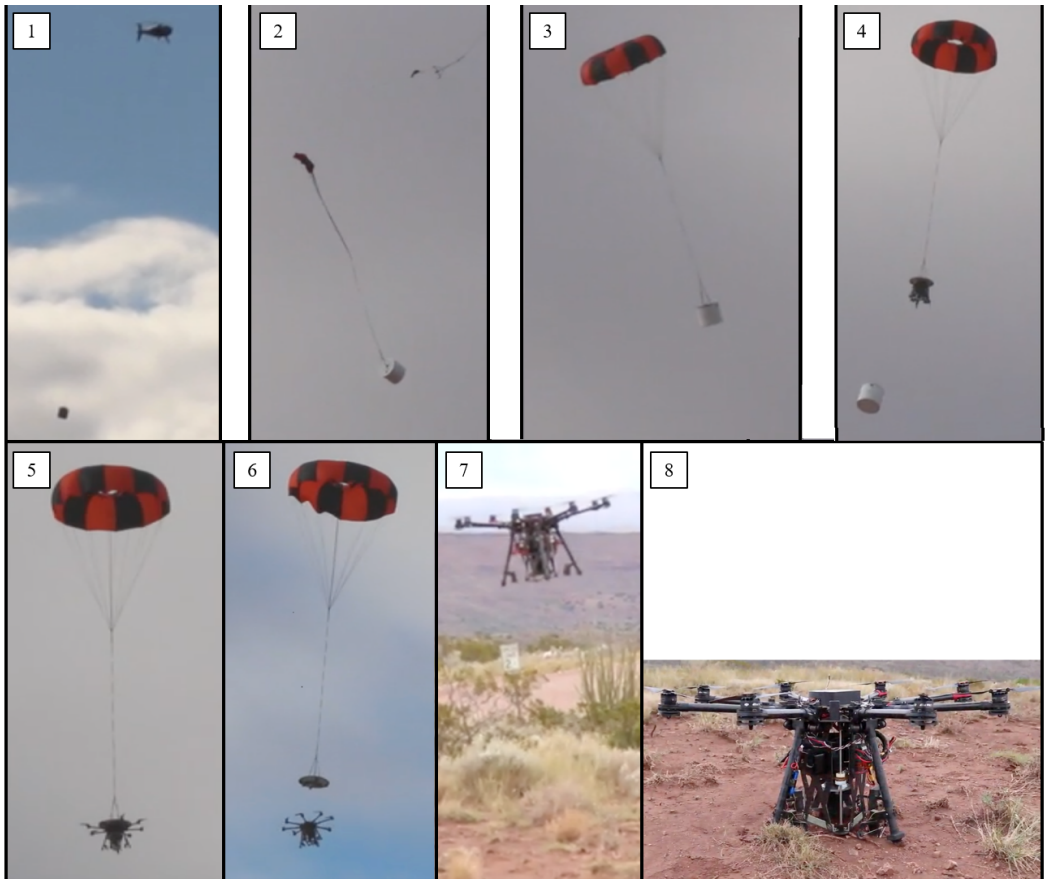

Figure 1. Airborne deployment sequence: 1 transport, 2 release, 3 parachute descent, 4 outer shell release, 5 motor arm opening, 6 separation/flight, 7 landing, 8 sensor emplacement

meet our deployment range requirements. A highly flexible approach to increasing the flight range of the system is to transport it over the bulk of its required deployment distance using a larger aircraft. This requires new capabilities and infrastructure to safely attach, transport, and release the system from another, and subsequently fly to the target location autonomously. Solving these challenges provides an enduring solution to overcoming range issues associated with small UAS.

In this work, we develop a long-range sensor emplacement multi-rotor UAS that can be carried and deployed from a larger UAS or manned aircraft. Figure 1 shows our approach. Sensor Emplacement Enhanced Deployment System (SEEDS) is a UAS with a sensor emplacement system in a self contained, compact canister that protects the system during transport and descent. The canister, designed to minimize drag, is 1 carried by a larger aircraft and 2 dropped at altitude when near the desired area. Once it is dropped, 3 a parachute is deployed from the canister, lowering it to a target altitude. When it reaches the desired altitude, 4 the canister is released, 5 the arms of the UAS unfold, and 6 the vehicle is released from the parachute. It then 7 autonomously navigates to the target location, scanning the target area to ensure it is safe to land. Once landed, 8 the UAS digs a hole in the ground to insert the sensor while continuously monitoring the digging process to ensure the sensor is successfully installed. After this deployment, landing, and emplacement sequence, the UAS still has a nearly full battery and can fly to a retrieval area. System recovery after sensor implantation is not the primary consideration. As the system is designed to be transported by an asset with much longer range, we accept that the multi-copter will not by be able to fly a significant distance after it completes the sensor emplacement. However, the system is designed to depart the

area after sensor release so as not to disturb the surrounding environment with its presence. Low-cost commercial off-the-shelf parts were used in the design of the system to the maximum extent possible in order reduce costs and allow for the idea of a certain amount of disposability.

Deploying underground sensors from a UAS in remote locations requires addressing a number of challenges. First, small UAS may not have sufficient flight range to fly from the starting location to the desired sensor location. As a result, other vehicles may be used for initial transport and launch. The theoretical and practical issues of launching UASs from trucks, ships, and other large aircraft have been previously examined. We take the latter approach and, as our system is a multicopter, we face the following challenges related to aircraft size, landing zone selection and sensor emplacement. For our application we have designed our system to be transportable either internal or external to the carrying aircraft. In either case, minimizing the overall footprint of our system is important and requires us to modify the basic air frame of our octocopter. A second challenge is identifying a landing zone for the UAS after deployment. There has been significant research in this area resulting in UASs successful selecting safe landing areas. Our work differs from these in that our approach leverages light-weight sensors and aims to identify a location that is good for digging in addition to landing. Finally, we must dig a hole with a UAS and insert the sensor into the soil. Most UAS systems developed to deploy sensors drop them on the surface. More related to our approach are ground-based robots designed for planetary exploration and drilling. Our system differs in that we use a non-percussive, adaptive augering mechanism to insert our sensor into the soil as opposed to collecting a sample of that soil.

In this article we present the design requirements that led to the development of the SEEDS long-range sensor emplacement UAS. We then detail the design we developed to address the requirements. We conducted a series of full-system field experiments where our UAS was deployed at high speed and altitude from a Schiebel S-100 in both Mesa, Arizona and at White Sands Missile Range. We used these experiments to iteratively refine our approach to increase the robustness to failures we saw in the harsh field testing environment.

In our prior work [Sun et al., 2018, Plowcha et al., 2018] we demonstrated using a UAS with an attached auger device to drill a sensor into the ground. This work differs from our prior work in four significant ways. First, our prior work required manual flight to the target location and could not be deployed from a larger aircraft. Second, our prior work did not have the ability to assess the landing location autonomously prior to landing. Third, we completely redesigned the UAS and emplacement system to carry larger sensors and to enable improved augering techniques. Finally, in this work we perform a number of in-situ experiments to stress test the performance of the SEEDS in representative environment.

In this article, we make the following contributions:

- The development of the requirements and the detailed description of the **complete** system capable of deploying a multicopter UAS over an arbitrary distance from a larger manned or unmanned aircraft.
- A lightweight laser scanning landing zone evaluation system that scans the potential target area and provides a rapid "go/no-go" decision.
- A UAS-mounted auger-style sensor emplacement system with improved capabilities over our previous work [Sun et al., 2018, Plowcha et al., 2018].
- Experimental evaluation of the SEEDS system with field results that highlight the success rates of the system when assessing the previously mentioned contributions.

We examined the success rates of each of our three contributions through a series of four geographically disparate field trials. The remainder of this work is organized as follows: Section 2 elaborates on related work and challenges; Section 3 highlights the requirements we outlined with feedback from stakeholders; Section 4 describes the approach and implementation details; Section 5 presents the results of our extensive field trials; and Section 6 concludes the work and identifies opportunities for improvement.

2. Related work

Our primary contribution is the convergence and integration of technologies for a deployable UAS enabling remote sensor emplacement. Given cost, disposability, and constrained Size, Weight, and Power (SWaP) requirements, limits on sensors and algorithms in some cases prevented leveraging state-of-the-art technologies. In other cases, state-of-the-art algorithms or components were unnecessary to meet requirements that could be met with lower-cost and/or proven strategies. Here, we review autonomous UAS range and sensor deployment, and landing zone selection and verification with a focus on low-cost, deployed systems with demonstrated success. We discuss how our system advances state-of-the-art deployable vehicles for in-ground sensor installation, and, where appropriate, extends individual algorithms or robotics foundations.

2.1. Deployable UAS range

While the maneuverability and hover capabilities of multicopters make them useful platforms for many tasks, their ability to remain airborne for extended periods of time (and consequently fly extended distances) pales in comparison to their fixed-wing counterparts. Commercially available offerings from companies like DJI and Foxtech with the required payload capabilities can remain airborne for $\sim$ 40 min [DJI, 2019, Foxtech, 2019]. However, adding a heavy payload can reduce this time to 10 minutes or less. Extending the range of this vehicle by extending its flight duration requires an energy-dense solution. Increasing batteries may improve this at the expense of additional weight leaving little for added payload. Hydrogen fuel cells have high energy density but currently cannot supply the instantaneous power needed for high-power multirotor propulsion [Lussier et al., 2019]. Lower energy-density solutions such as solar cells can currently only supplement another energy source but cannot replace them [Lussier et al., 2019]. A practical solution to extending flight range without increasing the vehicle's flight duration is to utilize another vehicle for long distance transport.

Getting UASs with limited ranges to their intended areas of operation can be challenging. Brungardt notes various examples of moving the launch point of the UAS closer to its target area [Brungardt, 2012]. If the vehicle is sufficiently small or compact, it can be human-carried to an area and hand-launched as is done with AeroEnvironment's RQ-11 Raven [AeroEnvironment RQ-11 Raven, 2019]. For larger UASs, a launching system can be mounted on an automobile [Planck Aerosystems, 2019]. When bodies of water afford a route close to the desired operating area, ships can also transport and launch UASs as is done with Northrop Grumman's Fire Scout and Insitu's Scan Eagle [Northrop Grumman Firescout, 2020, Insitu ScanEagle, 2020]. However, such vehicles are typically purpose-built, "turnkey" solutions that don't allow customization. To introduce new capability other vehicles must be utilized.

Weighing 11.3 kg and incapable of folding to a human-transportable size, our multirotor system cannot reasonably be carried by a person for any appreciable distance. Additionally, its 2 km range minimizes the utility of being transported and launched by either automobile or ship-based methods when the automobile or ship cannot get within the appropriate target distance. Simply put, it cannot fly far enough from a surface-based launch point to make it to its intended area. A solution allowing for closer-range deployment is an airborne deployment strategy similar to that proposed in [Bishop et al., 2010]. This allows us to deploy our system from another aircraft that is flying directly over our desired target area. Some success has been shown using such a strategy. Jo et al. demonstrate the deployment of a quadcopter from a larger, fixed-wing UAS [Jo et al., 2019]. The quadcopter was not contained or covered, however, and the risk of damage to sensitive on board equipment over an extended transport flight would be a significant concern in our case. We utilize a parachuting canister for our vehicle to keep it protected, increase the useful distance it can be transported, and preserve battery until it gets closer to the target. The U.S. Army has experimented with parachute-deployment of UASs via the Joint Precision Airdrop System [Klinkmueller et al., 2019]. Their proposed system is designed to launch multiple UASs which then go on to deliver

small payloads (2.27 kg to 6.8 kg) to the ground. Their launch mechanism is designed to be carried internally by a transporting aircraft, and their initial proof of concept testing consisted only of smaller 450 mm quadcopters that would deploy and land at various locations. [Klinkmueller et al., 2019]. Our full-size system is completely mission capable and can deploy, land, and insert its sensor payload into the ground. Additionally, it can be transported externally via sling, allowing it to be transported by aircraft with a limited amount of internal cargo space.

2.2. Landing zone selection and verification

Verifying the suitability of a landing zone from an airborne autonomous vehicle is a well-studied problem that encompasses numerous sensor types and analytical techniques. In a survey paper about guidance, navigation, and control of unmanned rotorcraft systems, Kendoul notes that the most popular sensors used for safe landing area detection are either vision-based or lidar-based – a precisely contrasting solution set [Kong et al., 2014,Kendoul, 2012]. That is, vision-based systems are relatively inexpensive to procure, add little weight to the UAS, but require significant computation to process images to obtain useful results. In contrast, lidar-based systems cost and weigh more than cameras, but provide data that requires less computation to be utilized.

In recent years, data fusion has led to techniques that combine both camera and laser scanner data to provide a more accurate representation of a landing area [Natividade et al., 2017,Singh et al., 2016,Lacerda et al., 2018]. For instance, [Johnson and Ivanov, 2011] uses flash lidar in combination with known terrain data derived from imagery to estimate position within 90 meters for lunar landings. A limiting requirement for our system is the minimal a priori information known about the selected target site, and the need to minimize computational resources to keep weight and power requirements down. As a result, a more fitting solution is a lidar-only approach similar to [Whalley et al., 2009] and [Scherer et al., 2012]. In both cases, the aircraft involved are much larger than our UAS and therefore can employ higher-quality lidar-based systems. [Scherer et al., 2012] use a full-size unmanned Boeing MH-6 Little Bird helicopter weighing 1,000 kg, while [Whalley et al., 2009] use a Yamaha RMAX unmanned helicopter that weighs 82.5 kg. Both of these systems have high-fidelity scanning lidars mounted to their nose that are used for navigation and path planning as well as landing zone analysis. The laser scanning system on the RMAX aircraft weighs 2.72 kg, which is $\sim 3/4$ our available payload. These approaches provide a detailed map of the landing area but consume more computing resources than we have available on our system. We require lidar as a final safety-check to make a "go/no-go" decision about landing based on whether obstacles are obstructing the landing site, or ground slope would impair the landing – a decision that can be made with a lower-cost, lightweight, and lower-fidelity lidar requiring far fewer computational resources. Our algorithm is focused on meeting our requirements to generate a decision with a single traversal of the point cloud data.

2.3. Autonomous sensor emplacement

Placing sensors via UAS has a diverse history. Because aircraft often employ extensive sensor suites, in some cases, the UAS *is the sensor*. Eubank et al. deployed an autonomous seaplane for persistent ocean surveillance utilizing the on board sensor suite to monitor ocean conditions, while maintaining a watch circle through repeated flight/drift cycles [Eubank et al., 2010,Meadows et al., 2009]. Islam et al. continuously measure the temperature and humidity of a column of atmosphere [Islam et al., 2019]. Ore et al. use UASs to measure properties of a column of water from the air [Ore and Detweiler, 2018]. Anthony et al. designed a UAS that could classify the hardness and type of ground based on the forces measured on the UAS as it landed [Anthony et al., 2015]. Others have created a UAS with spiked legs that penetrated the soil in order to measure seismic activity [Stewart et al., 2016].

Most sensor deployment via UASs is done by simply dropping sensors at a desired location. Usually this implies the sensors come to rest on top of the ground [Corke et al., 2006,Schwarzbach

Table 1. System requirements

Requirement	
Max Range	> 25 km
Max Deployment Altitude	3000 m
Max landing zone Slope	7°
Max # of landing zone Obstacles	Clear of obstacles
Autonomous re-planning in case of bad landing zone	yes
Min Sensor Depth	150 mm
Max Soil Compaction	0.4 MPa
Max Soil Moisture Content	40%
Max time spent digging	unspecified
Autonomous re-planning in case of failed dig	yes
Power required after insertion	Sufficient to reach rally point

et al., 2012, Pister, 2001]. However, for sea-based applications, Bradley et al. developed a system capable of dropping micro-buoys into the ocean near icebergs [Bradley et al., 2015].

Our approach differs from these methods in that our system 1) lands to place a sensor, 2) drills the sensor down in the ground, and 3) leaves the sensor after departure. We do this by employing an auger to drill the sensor into the surface. Remote drilling has been studied extensively, particularly in the realm of planetary exploration. This is usually done with a percussive drill with a hollow bit used for retrieving a core sample [Zacny and Cooper, 2006, Parness et al., 2012, Zacny et al., 2011, Shi et al., 2014]. The percussive drill uses a striking mechanism to apply a momentary vertical force on the rotational drill bit that increases drilling effectiveness without having to add additional weight on bit. Contrary to this, our goal is not to retrieve a core sample, but to place a sensor that is embedded in the auger into the soil. The limited amount of space and payload capacity prevent us from utilizing a percussive drill. In previous work we utilized a DC motor to rotate the auger and a passive spring system to apply weight on bit [Sun et al., 2018, Plowcha et al., 2018]. Here we have completely redesigned the augering mechanism to utilize a lead screw actuator to precisely control the travel of the auger, retract it when necessary, and apply weight on bit.

3. Requirements

Working with our collaborators within the U.S. Department of Defense (see the Acknowledgements section at the end of this work), we determined three primary requirements that dictated the overall design: 1) deployable UAS range, 2) autonomous identification and verification of landing zone, and 3) autonomous emplacement of the sensor. Currently we consider the system disposable and do not require a return to launch point. These requirements are summarized in Table 1 and summarized in more detail below.

3.1. Deployable UAS range

Our goal is to have a fully autonomous sensor emplacement system. The range of this UAV, fully loaded, was designed to be ~ 1 km, with the bulk of usable range beyond that distance coming from being carried by a larger aircraft. As such, once loaded, the usable deployment range is dependent upon the transport vehicle as long as it gets within ~ 1 km of the target site. Since our vehicle may be carried externally via cargo sling as well as internally, we also examine the requirement of understanding the effects of drag on our system while it is being transported in this manner. As an example application, we are using UAS to monitor wetlands in the San Joaquin river valley in California, USA. We aim to emplace sensors into various terrain in that area, and monitor these sensors over extended periods of time. Within the San Joaquin river valley, sensor implantation distances of up to 25 km from an initial launch point are required, but well beyond the capability of our loaded multicopter.

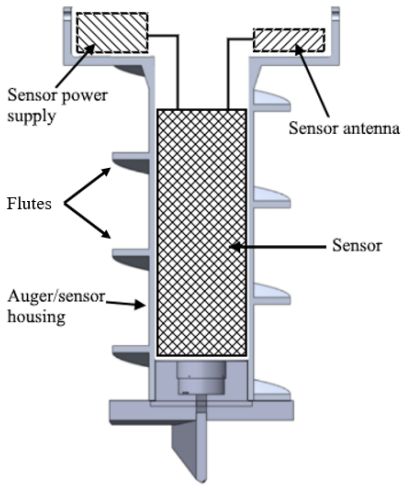

Figure 2. Cutaway of auger showing internal sensor placement - the auger along with the sensor are both left behind after the drilling process

3.2. Landing zone selection and verification

We identify the desired sensor region prior to launch and provide that location to the system as a GPS coordinate. We assume the target is chosen based on strategic needs and the corresponding landing zone is vetted for basic flatness and minimal obstacles. However, it is expected that errors in the selection process, including GPS error, could result in a target site with inadequate landing area (e.g., obstacles, unfavorable slope). As a result, we require the system to autonomously identify whether or not the landing area is unsafe and subsequently seek and select a more appropriate landing zone and verify it for sensor implantation. More precisely, we require the system to autonomously identify a landing zone with acceptable slope (see Section 4.2.1) and have no obstructions within a 2 m radius that would impede the aircraft's ability to land. In the event a landing zone is unsuitable, the system searches for a new one using a predefined search algorithm until a suitable landing area is found or the aircraft can no longer fly due to battery depletion.

3.3. Autonomous sensor emplacement

To simplify system design and operation the sensor is placed inside the auger, and the combined package is inserted into the soil and left behind. As a result, the size of the sensor and the requirement to place that sensor at the desired depth of 150 mm dictate the size of the auger. Based on discussions with our collaborators, we designed our emplacement system to accommodate a cylindrical sensor up to 100 mm in length with a maximum diameter of 35 mm. The sensor's power supply and antenna need not be a part of the main sensor body and could be placed in the top portion of the auger housing. This resulted in an auger shaft measuring 150 mm in length with a diameter of 40 mm (not including the auger flutes). The entire auger assembly is shown in Figure 2.

The type of soil, its moisture content, and compactness level determine the design of the auger bit and flutes, as well as the autonomy/controller operating the auger. As in our prior work, the target soil is of type 50% silty clay and 50% sand compacted up to 0.4 MPa, with a maximum moisture content of 40% [Sun et al., 2018].

Finally, the system should be capable of predicting installation success or failure relatively quickly in order to potentially relocate and try a new installation site. In our previous work [Plowcha et al., 2018], our sensor implantation system relied on gravity and the weight of the UAS to push the auger into the ground while it was rotating. With this method, we could predict the success of a sensor insertion evolution within 20 seconds of starting to auger. Our new sensor emplacement system relies

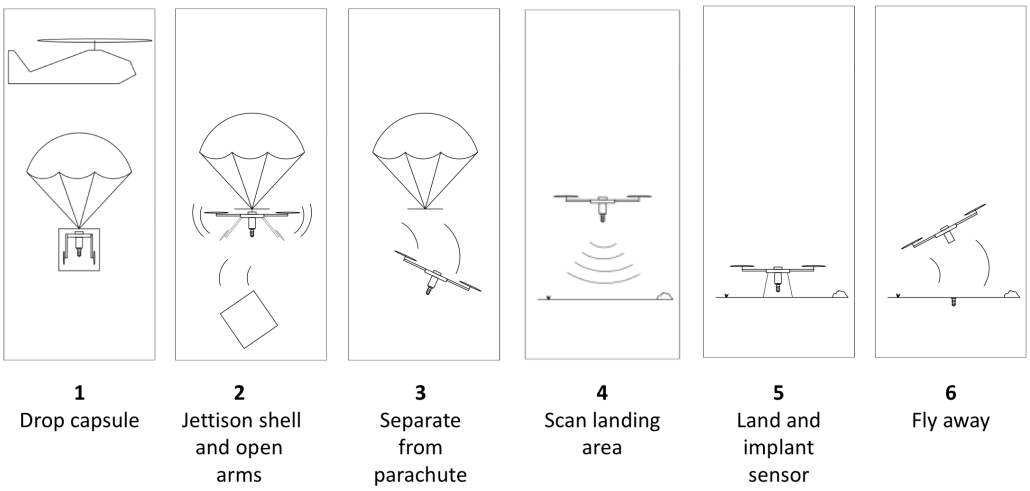

Figure 3. Deployment sequence

on an elevator mechanism to push the rotating auger into the ground. It takes 110 seconds for full traversal of the elevator assuming there are no impediments in the soil (i.e., roots, rocks, sections of high moisture, etc.). This rate of advance is slower than our previous system, so we increased our decision window to 40 s when determining whether to continue augering.

4. Approach

Figure 3 shows an overview of our approach used to meet the requirements specified in Section 3. To meet the first requirement, our approach consists of transporting a multicopter with attached sensor emplacement mechanism by another aircraft over the area where the sensor will implanted. Once over that area, the multicopter is dropped from the transporting aircraft (Figures 3.1 and 3.2) and descends via parachute to a predetermined altitude where it then detaches itself from the parachute (Figure 3.3) and flies to the precise location where the sensor is to be installed into the ground. After arriving in a hover over the desired location, the multicopter scans the landing zone (Figure 3.4), lands, drills the sensor (Figure 3.5) into the ground using an auger mechanism, and flies away when sensor emplacement is complete (Figure 3.6).

As in our previous works [Sun et al., 2018, Plowcha et al., 2018], we chose a multicopter as the means of sensor delivery. Multicopters can precisely land in confined areas that would otherwise be inaccessible to larger traditional or vertical takeoff and landing capable fixed wing aircraft. Their higher degree of maneuverability also allows for faster and more precise repositioning to a new location, should that be necessary. SEEDS is a complete redesign of our previous system. Our prior work used a DJI Matrice 100 built in to a frame that allowed the aircraft to slide up and down with the advance or retraction of the auger. SEEDS is based on the larger DJI S-1000 airframe and uses an elevator mechanism to drive the auger into the soil while the airframe remains in place on the ground. This allows almost the full weight of the multicopter to be transferred to the auger bit to aid in drilling, but also adds the additional requirement of countering the torque generated by the auger to prevent the multicopter from spinning. We prevent this spinning by using conical end caps on the landing gear that penetrate into the ground to keep the aircraft in position and by carefully balancing the amount of downward force. Once the auger and integral sensor are in place, the multicopter releases them and flies away from the area.

The remainder of this section provides greater detail about our approaches to extending the useful ranges of sensor employment, selecting and verifying our landing zone, and autonomously implanting a sensor into the soil.

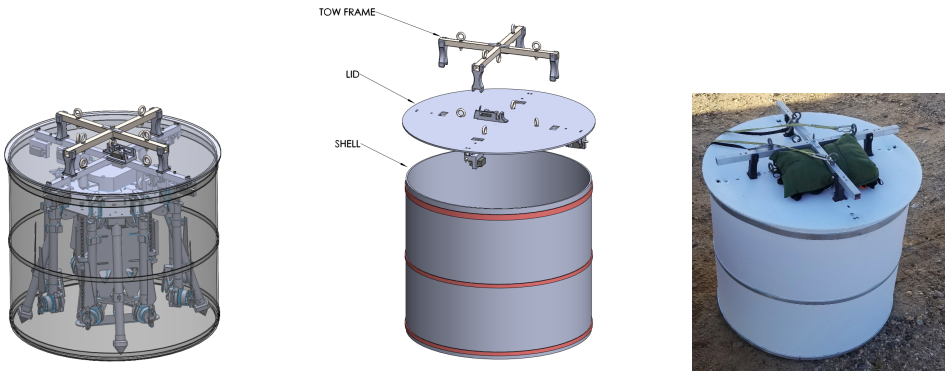

Figure 4. Containerized deployment system showing the design of the system's protective cover on the left and center with the actual fielded model shown on the right

4.1. Deployable UAS range approach

The first step in ensuring that a sensor can be autonomously inserted into the ground at an arbitrary distance from a launch point is transporting the system close enough to the desired sensor emplacement location. We took a two-part approach to this. First, we designed a containerized deployment system, with consideration for both reducing aerodynamic drag and adding protection, that can be transported by another aircraft, either inside a cargo area or externally attached. Once in the proper vicinity, the system can be dropped into a target area. Then, we modified our UAS so that it would fit inside our container and also be capable of autonomously controlling the entire deployment sequence of events.

4.1.1. Containerized deployment system

The containerized deployment system consists of two parts, a capsule and lid, that protect the UAS during transport and deployment operations (see Figure 4). The capsule is of a cylindrical design consisting of an aluminum frame with corrugated polypropylene walls and floor. It protects the UAS from wind effects, debris, and moisture during the transport and deployment process, as well as reducing drag for use during cargo sling operations.

The lid is an aluminum cross piece with servo-driven pin release mechanisms covered with corrugated polypropylene. Sway braces on the aluminum cross piece keep the UAS rigidly attached and prevent unnecessary movement during transport and deployment. For sling load operations, the lid attaches to a welded aluminum tow frame by a single-point release pin (the initial system design used a two-point release mechanism and is discussed in Section 6.1.1). The lid contains all of the electro-mechanical elements that control the deployment of the parachute (during free fall operations) or release from the tow frame (during sling load operations), the jettisoning of the outer shell, and the release of the UAS from the lid (see Figure 5).

The capsule can be deployed using a free-fall or a static-line method. If dropped via free-fall, the capsule trails a drogue parachute that deploys the main chute upon reaching a specified altitude. The static-line method pulls the main parachute from its housing as the capsule falls away from the transporting aircraft resulting in parachute-controlled descent immediately upon release from the tow frame.

The entire deployment sequence is based on altitude gates. As the capsule descends after being released from the transporting aircraft, actions are triggered as it passes through a sequence of predetermined altitudes. If deployed via free-fall, the initial altitude gate releases the main parachute. Once the main parachute is deployed, subsequent altitude gates trigger the following actions in order:

1. Jettison capsule shell
2. Open motor arms

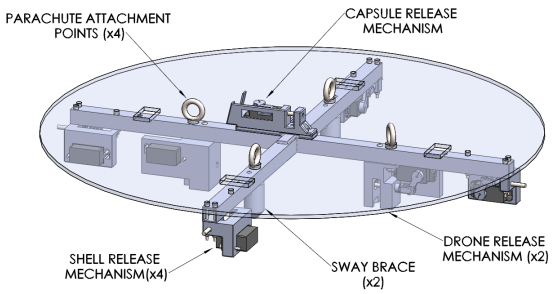

Figure 5. Containerized deployment system lid

3. Separate from parachute
4. Arrest descent and enter automatic flight mode

4.1.2. DJI S-1000 UAS with Pixhawk and primary computer

Our multicopter is a heavily modified DJI S-1000. The S-1000 is a commercially available octocopter marketed to aerial photography enthusiasts. Our version is outfitted with the open source hardware Pixhawk flight controller running the open source ArduPilot Mega flight control firmware stack.[1]

Figure 7 shows the changes we made to the base S-1000 airframe. In order to accommodate the mission, we either modified, added, or replaced the following items on our UAS:

- The T-style twin landing legs were replaced with four fixed landing legs with conical feet.
- The lower fuselage plate was replaced with a thicker carbon fiber one.
- The motor arm mounts were replaced with ones that used spring-loaded retention mechanisms.
- Motor arm deployment springs were added to automatically extend the motor arms during deployment.
- Motor arm deployment servos were added to actuate the arm release mechanism.
- The flight controller firmware was modified to accommodate our unique deployment and auger system requirements
- A laser scanner landing zone evaluation system was added.
- An elevator actuated auger system was added to the bottom of the thicker fuselage plate.

The S-1000 normally has "T-style" retractable landing gear. This is unsuitable for our purposes as this landing gear would not prevent the UAS from spinning counter to the torque generated by the auger mechanism as it penetrates the soil. Additionally, this landing gear was not compact enough to fit in our deployment container. We therefore refit the vehicle with four stationary landing legs with conically spiked feet that penetrate the ground and aid with anchoring the aircraft in place during auger operations.

To decrease the spatial footprint and allow the UAS to fit into the containerized deployment system, the fixed motor arm mounts were replaced with hinged mounts that allow the arms to be folded under spring tension from torsion springs and held in place against the landing legs via the motor arm deployment servos until the external protective container is jettisoned (see Figure 6).

We replaced the stock lower fuselage baseplate with a thicker carbon fiber variant capable of handling the stresses imposed by the spring arm deployment mechanism and the mounting of the elevator-actuated auger system. Figure 7 shows this and the other modifications of our S-1000 UAS.

Algorithm 1 describes our custom flight mode in the flight controller firmware, which controls all aspects of the automated deployment sequence. Servos actuate the various mechanisms that comprise the airborne deployment sequence and are connected to the auxiliary output control lines

[1] ArduCopter V3.8.0

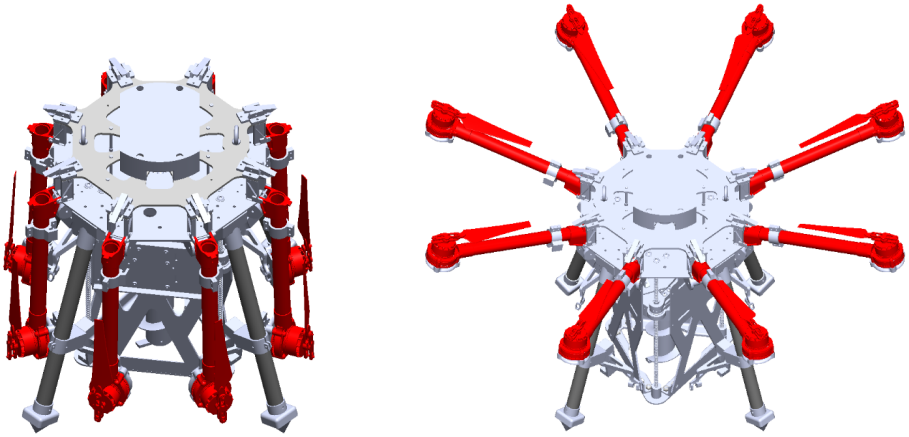

(a) Arms folded **(b)** Arms open

Figure 6. UAS motor arm modification with a) arms folded and b) arms extended after spring deployment mechanism actuation

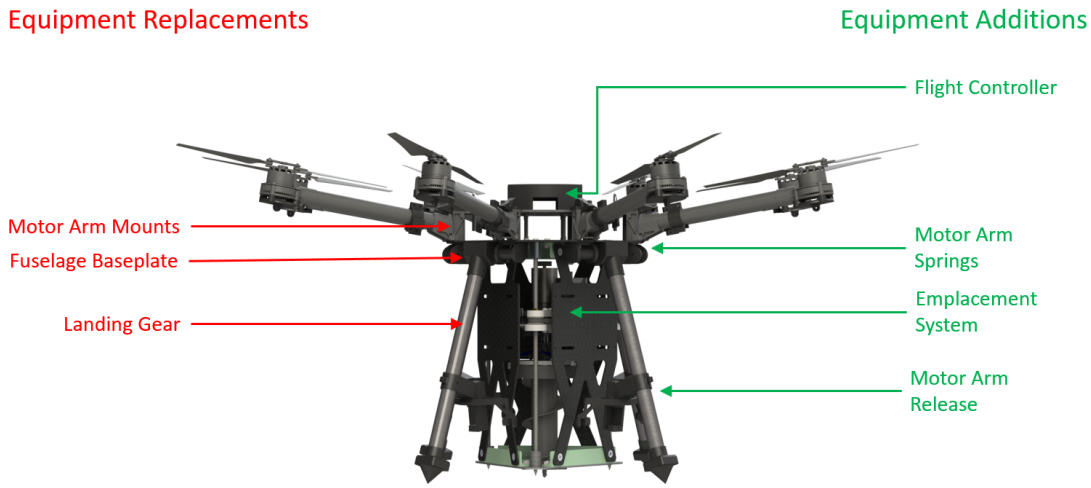

Figure 7. Modified S1000 - replacement parts are labeled in red, newly added parts are labeled in green

on the flight controller. In Algorithm 1 line 5, the flight mode is initialized and a user-selectable initial state of either free-fall or parachute descent is set. The free-fall state indicates that the container will be dropped from the carrying aircraft, and the main parachute will deploy upon reaching a target altitude. The parachute descent state indicates that a static line is attached from the carrying aircraft to the main parachute, and that the parachute will deploy immediately upon the container's release from the transporting aircraft. After initialization, the control loop portion of the flight mode executes at 400 Hz. Here the main state machine of the flight mode is executed in lines 9 through 21 of Algorithm 1. Each state change is triggered by a predetermined altitude gate and initiates a hardware response that advances the system to the next state. The flight controller's auxiliary output control lines are connected by a detachable harness to the servos that actuate the release mechanisms on the deployment container. This allows the UAS to separate cleanly from the parachute and capsule lid at the appropriate time. Additionally, we modified the automatic flight mode in the flight controller firmware to accommodate the serial communications required

Algorithm 1. Airborne deployment

```
1:  procedure DropMode
2:      // DropMode is a new flight mode added to the flight
3:      // controller to handle airborne deployment via parachute.
4:
5:      Initialize - called once when mode is first entered:
6:      state ← freefall // state can be freefall, parachute-descent, or powered-descent
7:
8:      Run - continuously called while mode is active:
9:      if state == freefall && altitude == parachute-deploy-altitude then
10:         openMainChuteServo();
11:         state ← parachute-descent;
12:     if state == parachute-descent then
13:         if altitude == container-release-altitude then
14:             openContainerReleaseServos();
15:         if altitude == arms-open-altitude then
16:             openArmSpringServos();
17:         if altitude == uas-separation-altitude then
18:             openTowFrameReleaseServo();
19:             armMotors();
20:             state ← powered-descent;
21:     if state == powered-descent && altitude == uas-recovery-altitude then
22:         arrestRateOfDescent();
23:         switchToAutoFlightMode(); // Auto flight mode flies the UAS to the digging location
```

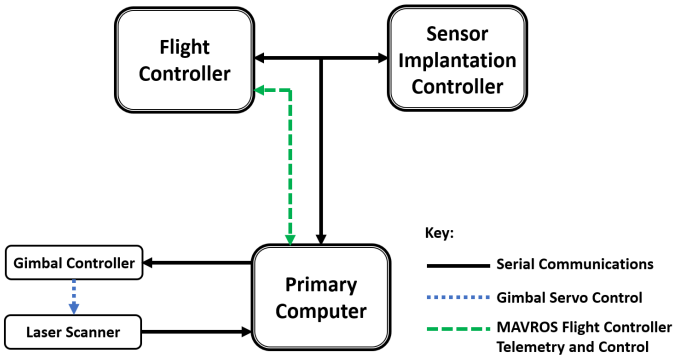

Figure 8. Computational systems and connections

between the flight controller, the sensor emplacement controller, and the primary system computer (see Figure 8). The primary computer also uses the Robot Operating System's MAVROS package for full-duplex communications with the flight controller via the Micro Air Vehicle Communication Protocol.[2]

Communication between the computational systems occurs as follows. When the UAS reaches the programmed sensor insertion location, the flight controller signals the primary computer to scan the landing zone. The flight controller waits for the scanning operation to complete and the primary computer to command either a landing, if the landing zone is suitable, or flight to a

[2] ROS Indigo Igloo compiled for the Raspberry Pi Zero with the MAVROS 0.33.0 package

new location, if it is not. Once a landing is complete, the flight controller then commands the sensor emplacement controller to commence emplacement operations. Depending on the outcome of the augering operation, one of two actions are performed. If sensor implantation is successful, the auger/sensor housing is released from the motor, the sensor emplacement controller signals success to the flight controller which then launches the UAS and flies to a predetermined scuttle location. If sensor insertion fails, the sensor emplacement controller retracts the auger/sensor housing, signals failure to the primary computer which then computes and loads the next potential sensor emplacement location into the flight controller. Once the flight controller receives this new flight plan, it launches the UAS and proceeds to the next potential area and begins the landing zone selection and verification process over again.

4.2. Landing zone selection and verification approach

After our UAS has been deployed over some distance and reaches the desired digging location, it must verify that the area beneath it is suitable for landing and subsequent sensor installation operations. Presumably, the location was chosen with some foreknowledge of the terrain and that it would be suitable for sensor implantation. However, variances in navigation due to inherent satellite navigation error or changes in terrain due to natural events such as falling trees, rock or mud slides, flooding, and so on, may mean the UAS ends up hovering over an unsuitable landing zone.

In order to evaluate the suitability of the landing zone, we developed a laser scanner system to generate a point cloud of elevation values for the area beneath the UAS. The laser scanner is our sensor of choice as it provides more detailed information than sonic sensors and the analysis of the resultant point cloud takes fewer resources than those used by other methods such as binocular stereo vision. Additionally, the laser scanner works at night or in low-light conditions which would otherwise negate the use of computer vision techniques.

We use a servo-mounted Hokuyo URG-04LX-UG01 laser range finder that is stabilized along its pitch axis to scan the area immediately under the UAS prior to landing. The scanning system is mounted on the elevator chassis and provides a 50 degree by 50 degree field of view of the landing zone. It is shown in Figure 9 and can scan the area under the UAS in 4.32 seconds. The resolution of the laser range finder combined with the field of view provided by the servo results in a point cloud of 144 by 144, or 20,736, height values representing the terrain underneath the UAS. This point cloud is generated once the aircraft is in a stable hover over the landing zone. While there may be minor adjustments to the aircraft's position and attitude as it maintains its hover location, we accept these resultant perturbations in the scanner data as the overall goal is to simply determine if there is significant terrain differential which will preclude a safe landing.

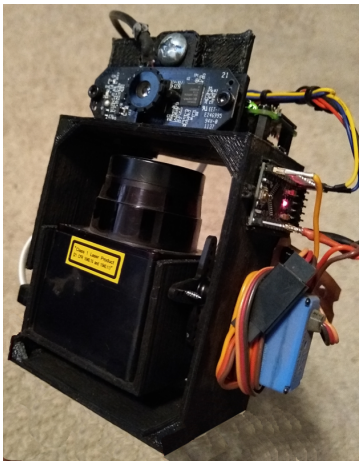

Figure 9. Landing zone evaluation scanner

Algorithm 2. Landing zone evaluation scanner analysis

```
1:  procedure AnalyzeLaserData
2:      fixCorners();
3:      linearInterpolate(LEFT-EDGE);
4:      linearInterpolate(RIGHT-EDGE);
5:      // We now iterate through the point cloud row by row.
6:      i ← 0;
7:      while i < number of point cloud rows do
8:          linearInterpolate(ROW[i]);
9:          i ← i + 1;
10:     // Store values needed to analyze area.
11:     min ← findMin();
12:     max ← findMax();
13:     delta ← max − min;
14:     slope ← calculateSlope(min, max);
15:     // Return landing zone status
16:     if delta > maxAllowableDelta OR slope > maxAllowableSlope then
17:         return BAD-LANDING-ZONE;
18:     else
19:         return GOOD-LANDING-ZONE;
```

Since laser scanners can generate erroneous returns depending on the environmental conditions [Nie et al., 2017], it is necessary to ensure that reasonable values have been returned by the system prior to determining the validity of landing zone. Algorithm 2 describes how we filter any invalid data returned from the laser scanner and determine if the landing area is safe.

The laser scanner returns three types of invalid data values: "infinity," "not a number," and negative values. As these types of values can cause an invalid landing zone determination calculation, we convert them to valid information after the scan process is complete. In line 2 of Algorithm 2, we check if any of the corners of our point cloud contain invalid data. If so, we replace their values with the nearest neighbor that contains valid data. By ensuring valid corner data, we can then replace any invalid data down the left and right edges using linear interpolation as shown in lines 3 and 4 of Algorithm 2. This in turn allows us in lines 7 through 9 of Algorithm 2 to linearly interpolate our horizontal laser scan lines as needed to replace any remaining invalid data points. We use linear interpolation as opposed to other methods such as inverse distance weighting or linear least squares interpolation as this method performs faster on our computing platform than the other methods and still provides sufficiently accurate information for analysis.

Once we have filtered our laser scanner data, lines 11 through 14 of Algorithm 2 examine the differences between the values to determine the height of any obstacles or the overall slope of the landing zone.

If the laser scanning process reveals a suitable landing zone, then the UAS lands. Otherwise, the UAS executes one of two user-chosen search patterns in an attempt to find a suitable landing zone: a linear search or an expanding triangle search. Both searches continually push the UAS outward from its initially desired sensor emplacement location at distances selected by the user. The linear search does this in a single direction, while the triangle search positions the UAS at 120° points on expanding concentric circles, again at user-selected distances (see Figure 10).

These search types are chosen during mission planning based on the terrain in the landing zone. In general, if the area around the landing zone is thought to be relatively clear of debris, of acceptable ground slope, and with potentially permissive soil, then the triangle search is a useful option. In more constrained situations, seeking a new landing zone in only a single direction may be the only option available so a linear search would be chosen.

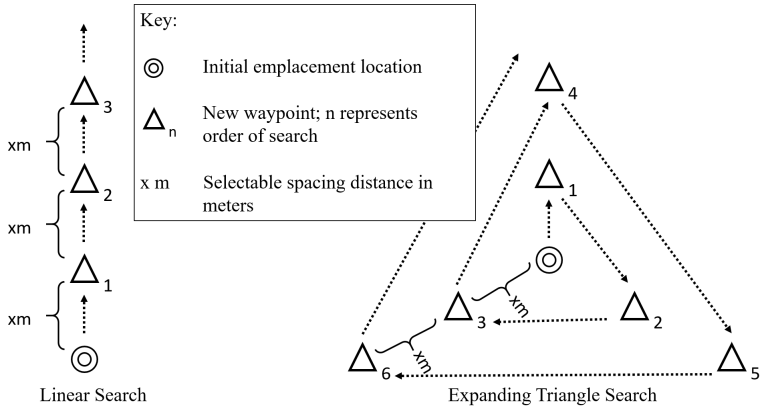

Figure 10. User-selectable search patterns chosen prior to flight which are used to find a suitable landing area if the current landing area is not viable

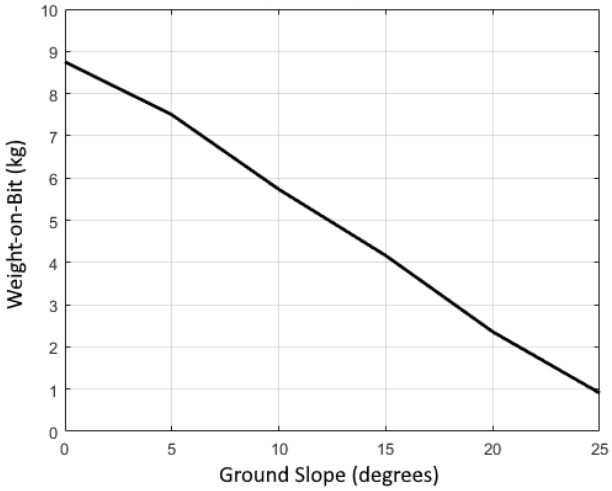

Figure 11. Effective weight on bit vs. ground slope

4.2.1. Determining slope requirements

Normally the concern with sloped ground and a UAS is the question of whether or not the aircraft can remain upright. If the UAS' center of gravity moves laterally beyond one of its ground contact points (e.g. landing gear), then it will simply fall over, an occurrence known as static rollover [Lobik, 1998]. The experimentally verified static rollover angle of our auger-equipped UAS is 26°.

However, we have a greater concern than simply not falling over. Our system needs to be able to insert a sensor into the ground, and it does this by driving an auger downward with the weight of the UAS behind it. This is known as weight on bit (WOB) and is a critical part of augering into soil as we demonstrated in [Sun et al., 2018]. In order to determine how much WOB our system could supply at different angles, we placed our UAS on a tiltable platform and measured the amount of effective downward force it generated on a sensor over an increasing series of slopes from 0° (level) to 25°. We define "effective downward force" as the amount of force with which the auger can be pressed downward prior to two or more of the landing gear breaking contact with the ground. The moment that two or more landing gear are no longer in contact with the ground, the torque generated by the auger motor will cause the entire UAS/auger system to spin about the axis of the auger bit and become unstable. Figure 11 shows the results of our effective WOB determination.

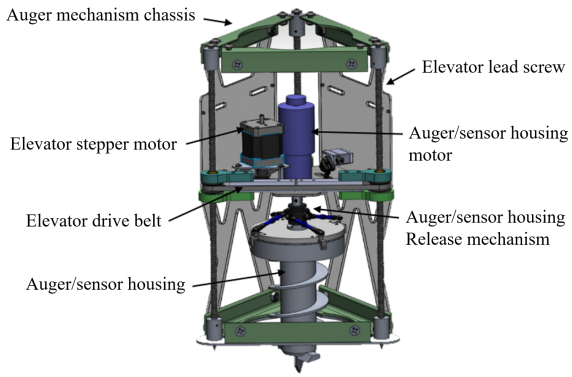

Figure 12. Cutaway view of the electro-mechanical auger system that is mounted to the underside of the aircraft

As we never exactly know how permissive a column of soil will be for augering operations, we chose a conservative 7° as our slope landing limit. This allows our auger mechanism to use the majority of the system's weight for sensor emplacement as well as providing a safety buffer for any unforeseen issues related to slope. For instance, striking a larger rock while augering can cause the entire system to momentarily break contact with the ground. At higher slopes, this could lead to a rollover scenario.

4.3. Autonomous sensor emplacement approach

Once the UAS has been carried to its area of operations, deployed, and landed, it must insert its sensor payload into the ground. To do this, an augering system is attached to the base plate of the UAS. It consists of an elevator platform (Figure 12), three lead screws that move the elevator platform via stepper motor, a DC motor that turns the auger bit containing the desired sensor package, and a release mechanism that detaches the bit from the digging system so that it may remain in the ground at the completion of an emplacement evolution. The augering system is controlled by a micro-controller that sends control signals to the stepper motor driver and the DC auger motor driver to control the position of the elevator platform and the speed/direction of the auger bit. The micro-controller receives motor velocity and current feedback to inform the software that controls the overall sensor implantation process.

The auger bit is a 3D printed cylindrical sensor housing with a cutting tip and helical flutes designed to break up and displace the soil as the bit advances downward. The large cylindrical area at the top of the auger remains above the ground and can be used for additional sensor components such as antennas.

In our previous work we show a generalized representation of auger performance in soil [Plowcha et al., 2018]. Figure 13 shows how as an auger increases depth in a column of soil a commensurate increase in motor current and decrease in auger RPM result. Understanding this general performance allows us to implement an intelligent algorithm to control our augering process. Unlike our previous sensor-installing UAS [Sun et al., 2018, Plowcha et al., 2018], this elevator-driven auger platform permits the partial or total retraction of the auger from the soil. This allows us to implement a technique known as pecking, a method where the auger is temporarily raised away from the bottom of the hole to allow chips or debris to be more easily transported up the auger flutes before advancing the auger bit further downward [Mellinger et al., 2002, Fujishima et al., 2000].

Algorithm 3 controls all aspects of our sensor emplacement system and reports the success or failure of that evolution back to the controlling computer. Line 3 of Algorithm 3 monitors the depth of the auger bit in the soil and time spent augering in conjunction with the motor current draw and auger shaft RPM to control the advance or retreat of the elevator platform. Line 4 of Algorithm 3 checks if motor current draw and shaft RPM exceed the predetermined threshold, or if

Algorithm 3. Sensor emplacement

```
1:  procedure EMPLACESENSOR
2:      currentState ← advancing;
3:      while !targetDepthAchieved || !timeLimitExceeded do
4:          if motorCurrent > currentLimit || shaftRPM < rpmLimit || shaftAdvance == false
    then
5:              //Pecking maneuver.
6:              currentState ← partialRetraction;
7:          if targetDepthAchieved then
8:              currentState ← fullRetraction;
9:              return SUCCESSFUL-EMPLACEMENT;
10:         if timeLimitExceeded then
11:             currentState ← fullRetraction;
12:             return FAILED-EMPLACEMENT;
```

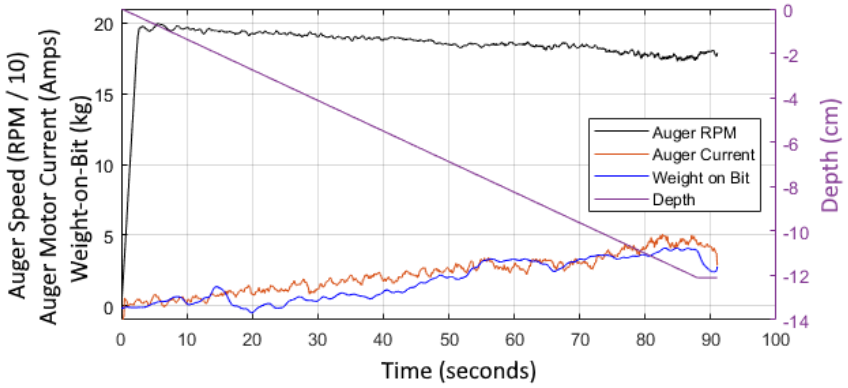

Figure 13. Auger performance classification - the system records auger RPM, auger motor current, weight on auger bit, and depth at a rate of 20 Hz

the depth of the auger ceases to advance. If these conditions are met, pecking occurs where the auger is momentarily retracted to allow debris to clear before further downward progress is attempted. Lines 7 through 9 of Algorithm 3 check if the target depth is achieved and respond accordingly by releasing the auger (which also contains the desired sensor), raising the auger platform, and signalling the main computer of the success. Lines 10 through 12 of Algorithm 3 handle the condition where the predetermined augering time limit is exceed by fully retracting the augering platform with the auger still attached and signaling the failure of the sensor insertion attempt to the main computer. In this case, the UAS launches and seeks a new location.

5. Experimental setup

Between September 2018 and May 2019 we evaluated the SEEDS system through four field experiments in four geographically diverse areas each having unique soil characteristics. Due to the logistical complexities involved in coordinating an additional air transportation vehicle, we evaluated SEEDS' functional subsystems (airborne deployment, landing zone evaluation, and sensor implantation) either individually or in conjunction with other subsystems in each experiment. Federal Aviation Administration regulations concerning UAS overall weight required us to coordinate the use of restricted airspaces in experiments one and two. Details of each experiment are given below and Table 2 provides a summary.

Table 2. Field experiment summary

Experiment Number	Location	Subsystem Tests: Airborne Deployment	Subsystem Tests: Landing Zone Evaluation	Subsystem Tests: Sensor Emplacement	Notes
1	Mesa, AZ	4	0	0	Initial integration testing with Schiebel S-100
2	Alamogordo, NM	6	0	4	Follow-on long range deployment testing
3	Lincoln, NE	0	38	10	Field trials focusing on evaluation of landing zone evaluation system
4	Nacimiento, CA	0	25	13	Integration of landing zone evaluation and sensor emplacement systems

(a) Foxtech Gaia heavy lift hexacopter **(b)** Schiebel S-100

Figure 14. Transporting aircraft - The two vehicles used to transport SEEDS during our testing periods

5.1. Experiment 1

Five initial tests of the deployment system were conducted in the vicinity of Mesa, Arizona on 9-11 September 2018. The test site field elevation was 530 m above mean sea level with all tests conducted between 114.8 m and 245.9 m above the field location. We conducted five airborne deployment tests during those three days with winds averaging from the southwest at 3.4 m/s and temperatures ranging from 32.3°C to 38.3°C.

The first deployment of SEEDS in Mesa, AZ, occurred from a Foxtech Gaia 160-MP heavy lift hexacopter (see Figure 14(a)). The Foxtech Gaia 160-MP is a heavy lift hexacopter that can carry a maximum payload of 30 kg. It has an overall height of 0.8 m and maximum rotor diameter of 1.6 m. While carrying SEEDS, which weighs 12.7 kg, this aircraft could remain airborne for 10 minutes.

All subsequent airborne deployments during this experiment period and the next were conducted with a Schiebel S-100 (see Figure 14(b)). The Schiebel S-100 is a gasoline-powered, rotary engine-driven unmanned helicopter system with a takeoff weight of 200 kg when fully fueled. The fuselage is 3.11 m long with a rotor diameter of 3.4 m, and its maximum cargo weight is 50 kg. It has a maximum sustained airspeed of 222 km/h with a maximum endurance airspeed of 102 km/h enabling it to remain aloft for greater than six hours while carrying SEEDS.

5.2. Experiment 2

Six airborne deployments from the Schiebel S-100 were conducted at the White Sands Missile Range in the mountains of Alamogordo, New Mexico. The first was conducted on 16 September 2018. Winds on the day of this test were from the southwest at 3.58 m/s with the temperature at 18.3°C. The remainder of the trials conducted as part of this experiment period occurred from 14-16 October 2018. On 14 October, winds were from the west at an average of 6 m/s with temperatures averaging 15.6°C. The remaining two days of testing had winds from the southeast at an average of 7 m/s and an average temperature of 5.23°C. All six of these tests focused on longer transport distances that ranged from 5-25 km with deployments occurring up to 2,402.8 m above the takeoff elevation. During this experiment any successful airborne deployments (i.e., successful jettison of SEEDS from the carrier aircraft) culminated in additional tests of the sensor emplacement system.

5.3. Experiment 3

From 1-12 April 2019, we conducted 38 flights at the University of Nebraska-Lincoln's outdoor flying area. Obstacles were randomly arranged in landing areas in order to test the landing zone evaluation system as well as evaluate the aircraft's ability to perform the search patterns depicted in Figure 10 when the landing zone was occluded. Additionally, we conducted 10 trials of our autonomous sensor insertion system in this same location.

5.4. Experiment 4

From 29 April to 3 May 2019 we conducted 25 flights testing both the landing zone evaluation and sensor implantation systems at the Camp Roberts Army National Guard base outside of Nacimiento, California, as part of the Joint Interagency Field Experimentation exercise.[3]

6. Results

The following section details our observations from testing the subsystems for airborne deployment, landing zone selection and verification, and autonomous sensor insertion over our four experimental periods. We organize the results by subsystem and note the experimental period or periods in which the systems were tested.

6.1. Airborne deployment

Airborne deployment consists of four phases: tow-frame release, outer-shell jettison, motor-arm deployment, and parachute release. After these four phases successfully complete, the aircraft autonomously flies to the desired landing zone, where the next subsystem, landing zone validation, is engaged. Experiments 1 and 2 tested the airborne deployment subsystem over the course of 11 total trials conducted in the deserts of Mesa, Arizona, and the mountains of Alamogordo, New Mexico.

Due to the configurations of our transporting aircraft, our sensor installing UAS was tethered beneath the transport and released using a static-line parachute up to 25 km away from the initial take-off point. This means the parachute was attached to the tow frame by a line that pulled the parachute from its bag as the container fell.

6.1.1. Release from tow frame

Release from the tow frame occurs when the flight controller sends a signal to a servo that withdraws a steel pin from a retention ring on the tow frame. We subsequently refer to this as a pin-pull mechanism. During our trials we evaluated two types of pin-pull release mechanisms: two-point

[3] https://nps.edu/web/fx

Table 3. Tow frame release results summary by experiment period -"Release Success" indicates whether or not the container successfully detached from the transporting aircraft

Experiment	Trial	Location	Temperature - °C	Windspeed	Carrying Aircraft	Release Mechanism	Release Altitude - HAT*	Airspeed	Inclination	Release Success
1	1	Mesa, AZ	33.0°	2.24 m/s	Hexacopter	2-Point	114.8 m	4.08 m/s	24.1°	Yes
1	2	Mesa, AZ	35.2°	3.35 m/s	S-100	2-Point	245.9 m	34.07 m/s	48.8°	Yes
1	3	Mesa, AZ	37.4°	5.36 m/s	S-100	2-Point	159.1 m	28.01 m/s	50.3°	No
1	4	Mesa, AZ	32.2°	2.91 m/s	S-100	2-Point	125.5 m	9.15 m/s	4.3°	Yes
1	5	Mesa, AZ	38.3°	3.13 m/s	S-100	2-Point	142.2 m	22.01 m/s	32.6°	Yes
2	6	Alamogordo, NM	18.3°	3.58 m/s	S-100	2-Point	2427.0 m	19.21 m/s	36.0°	No
2	7	Alamogordo, NM	14.4°	6.26 m/s	S-100	1-Point	1508.0 m	23.76 m/s	23.2°	Yes
2	8	Alamogordo, NM	16.8°	5.81 m/s	S-100	1-Point	2402.8 m	24.54 m/s	43.2°	Yes
2	9	Alamogordo, NM	3.7°	6.71 m/s	S-100	1-Point	1998.8 m	15.87 m/s	5.4°	Yes
2	10	Alamogordo, NM	6.6°	7.15 m/s	S-100	1-Point	1960.7 m	17.32 m/s	3.1°	Yes
2	11	Alamogordo, NM	5.4°	7.15 m/s	S-100	1-Point	1918.1 m	17.10 m/s	11.7°	Yes

*Height Above Takeoff

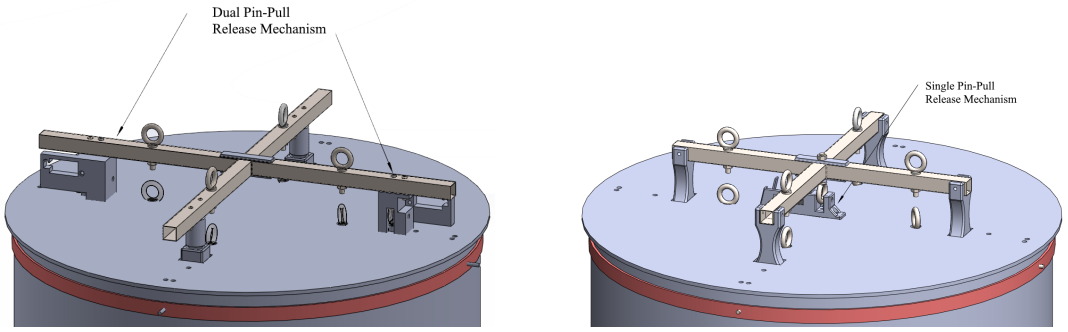

(a) 2-Point Release **(b)** 1-Point Release

Figure 15. Tow frame release mechanisms

and one-point (Figure 15). The summary of our tow frame release results are shown in Table 3. It details which experiment period, the location of the experiment, the transporting aircraft, the type of release mechanism, the release altitude in terms of height above takeoff (HAT), airspeed at time of release, and the inclination of the container in degrees at time of release. Ultimately, we found that the one-point release mechanism yielded far better results. Details of the issues and design decisions that lead to this conclusion are summarized in Appendix B.

Over 11 trials, we had 9 successful releases from the tow frame. For this subsystem, that is an overall success rate of 81.8%. The two failures resulted from either container inclination at time of release or excessive force placed upon the pin-pull mechanism due to a combination of airspeed and inclination.

6.1.2. Outer-shell jettison

At the predetermined altitude, the outer shell is jettisoned when the flight controller sends a pulse width modulated signal to retract the pins holding the outer-shell to the lid. In our field trials, these

Table 4. Outer shell jettison results - "Jettison Success" indicates whether or not the protective shell successfully dropped free from the container

Experiment	Trial	Location	Jettison Success
1	1	Mesa, AZ	Yes
1	2	Mesa, AZ	Yes
1	4	Mesa, AZ	Yes
1	5	Mesa, AZ	Yes
2	6	Alamogordo, NM	Yes
2	7	Alamogordo, NM	Yes
2	8	Alamogordo, NM	Yes
2	9	Alamogordo, NM	No
2	10	Alamogordo, NM	No
2	11	Alamogordo, NM	Yes

pin-pull mechanisms did not fail; however, in two instances during Experiment 2 the outer shell did not jettison correctly upon receiving the command to do so.

The third trial from Experiment 1 has been omitted from Table 4, as the capsule failed to separate from the tow frame. After multiple attempts to get the system to work, it was turned off in preparation for the S-100's return to base. Along its route home, the S-100 carried the capsule beyond the radio range of our control systems. At some point the S-100 slowed down and our package fell free and began a parachuted descent outside the range of any of our communications systems. As a result, we were unable put the system back into a state where it could autonomously jettison its shell; nor was it close enough to receive any manual inputs to command the same.

During two of tests in Experiment 2 (trials nine and 10), the altitude gate chosen to jettison the outer shell was too close to the altitude gate chosen to spring open the motor arms. Therefore the command to open the motor arms was sent before the shell fell clear of the bottom of the arms. The motor arms opened against the inner wall of the shell thereby holding it in place. Of the 10 trials where the outer shell jettison was tested, there were 8 successful instances where the outer shell dropped free of the container. This results in an outer shell release success rate of 80%.

6.1.3. Motor-arm unfolding

The eight motor arms are folded downward against torsion spring tension and held in place by four pin-pull mechanisms actuated by a signal from the flight controller at the appropriate altitude gate. On that signal, the torsion springs extend the arms into the fully open position and into their spring-loaded locking mechanisms.

The only failures of this system coincided with the outer shell jettison failures described previously and shown in Table 4. However, the release mechanism itself functioned as designed 100% of the time over the course of both Experiments 1 and 2. Additionally, during our initial development and testing we noted instances where a torsion spring would not fully extend a motor arm into its retaining mechanism. However, as noted in [Henderson et al., 2017] with a similar spring-arm mechanism, once power was applied to the motors, the resultant lift was sufficient to pull that particular motor arm into the correct locked position therefore providing redundant capability should the torsion spring fail to provide sufficient force to unfold the arm completely.

6.1.4. Release from parachute

The UAS is held to the lid of the container and, consequently, to the parachute, by a dual pin-pull mechanism. The flight controller actuates this mechanism by a signal when the UAS is at the predetermined altitude. We show a 100% success rate for this subsystem. In all instances where the flight controller sent the command to release the UAS from the parachuting lid, the UAS successfully separated, engaged its motors, arrested its descent at the desired altitude, and flew the appropriate user-selected flight plan to the designated sensor-emplacement location.

6.1.5. Airborne deployment success summary

We define overall deployment as successful when SEEDS exits or detaches from the transporting aircraft and arrives over its intended point of landing. Of the 10 trials where our system successfully detached from the transporting aircraft, we observed only two failures of the system to reach the desired area, and these were due to the outer shell of the container failing to separate (see Section 6.1.2). Therefore SEEDS successfully deployed from another airborne asset 80% of the time.

6.2. Landing zone selection and verification

Before we could verify the suitability of a landing zone with our laser scanner, we needed to determine the conditions that would be detrimental to sensor insertion operations. Large obstacles that could cause the UAS to tip over are clearly "no-go" criteria, but we also needed to determine how much ground slope we could land on and how that would affect our augering operations.

6.2.1. Landing zone evaluation scanner

We were able to conduct numerous tests of our landing zone evaluation scanner as that system did not require a larger transport asset or specific area where special permissions were required as was the case with the system deployment testing. Experiments 3 and 4 consisted of 63 trials of the landing zone selection and verification system. For Experiment 3 we conducted 38 flight tests of the landing zone evaluation scanner at the University of Nebraska's outdoor flight test area. Over the four day period of Experiment 4, we conducted 25 flight tests at Camp Roberts Army National Guard base in California as part of Joint Interagency Field Experiment 2-19.

We evaluated the system on its ability to distinguish suitable landing zones from unsuitable ones in terms of acceptable ground slope and/or obstacle content. In cases where natural obstacles were not present in our test zones, we artificially obscured our landing zone with cardboard boxes, Pelican™ cases, and field chairs. We define success and failure of the system in the following manner.

- SUCCESS: True Positive - the system correctly identifies a good landing zone
- SUCCESS: True Negative - the system correctly identifies a bad landing zone
- FAILURE: False Positive - the system incorrectly identifies a bad landing zone as a good one
- FAILURE: False Negative - the system incorrectly identifies a good landing zone as a bad one

We note that true positive and true negative situations are easily identifiable by an observer. It is self-evident if the UAS lands in an obstacle-free and flat landing zone. An observer can also easily tell if the UAS lands on an obstacle or tips over due to ground slope after landing. True negative results can also be intuitive if there are obstacles visible underneath the UAS; however, it is possible to confuse a true negative with a false negative, especially in terms of slope. If the UAS does not land in an area that appears clear, is it because the slope was out of limits or because there was an error in the scanning process? As observers were unable to get directly beneath the UAS while it was scanning (due to both logical and safety related reasons), it was difficult to differentiate between the two cases in some instances.

We present the results of 59 out of the 63 tests performed in Experiments 3 and 4 in Table 5, as on our flight tests in Experiment 4, our laser scanner overheated and failed to return any data. We show top-down imagery and the associated point clouds for both true positive and true negative examples (see Figures 16 and 17).

With 53 out of 59 landing zone scans correctly determining a valid go/no-go determination, we realize an overall landing zone evaluation success rate of 89.8% with a false positive rate of 17.6%. Two of the three false-positives that occurred during testing failed to identify an obstacle, while the third, shown in Figure 18, failed to correctly identify an area of excessive slope.

Finally, certain environmental conditions were found to lead to sub-optimal landing zone evaluation performance. Areas of tall grass (usually greater than 0.5 meters) would always be evaluated as unsuitable landing zones as variations in laser return height appeared as obstacles to the system.

Table 5. Landing zone evaluation success/failure analysis over 59 trials

	Success		Failure	
	True Positive	**True Negative**	**False Positive**	**False Negative**
Experiment 3	25	9	2	2
Experiment 4	14	5	1	1
Overall	39	14	3	3
Totals	53		6	

(a) Landing zone image **(b)** Landing zone scan

Figure 16. True positive: Visual image (a) and LIDAR data (b) depicting a clear landing zone

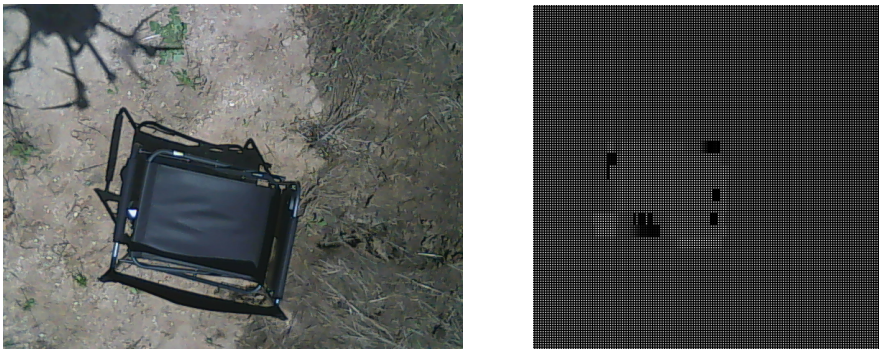

(a) Landing zone image **(b)** Landing zone scan

Figure 17. True negative: Visual image (a) and LIDAR Data (b) depicting an obstacle (field chair) occluding the landing zone

Also, puddles of water appeared as either flat areas or as invalid laser returns that were converted to valid returns by the interpolation smoothing portion of the algorithm. Working correctly, the system should identify those areas as unacceptable due to the unknown nature of the terrain beneath the water's surface.

6.3. Autonomous sensor emplacement

Experiments 2, 3, and 4 allowed us to evaluate our autonomous sensor implantation subsystem over the course of 27 trials in three distinct soil types. In our previous work, we note that unconfined compressive strength and moisture content are the main factors in determining the ease of augering operations followed by the actual soil composition in terms of sand, silt, and clay. [Sun et al., 2018].

Figure 18. False positive: Poor slope identification resulting in unsuccessful sensor implantation

Table 6. Average soil types per experiment

Experiment	Location	Moisture	Compressive Strength	Composition
2	Alamogordo, NM	35%-55%	0.65 MPa	Sandy, Clay, Rocky
3	Lincoln, NE	45%-60%	0.6 MPa	Silty clay, Sandy
4	Nacimiento, CA	20%-30%	0.7 MPa	Sandy, Rocky, Minimal clay

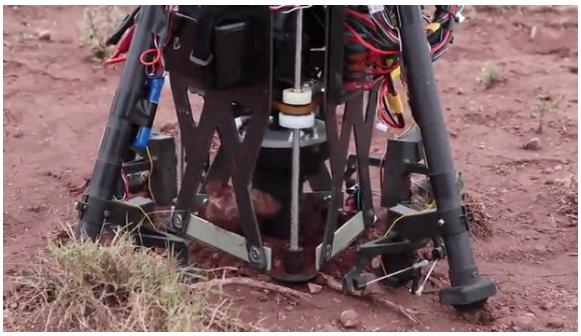

Figure 19. White Sands Missile Range rocky terrain

Unconfined compressive strength is the amount of amount of force required to crush or displace the soil within a given area, which parameter we express in terms of megapascals (MPa) [Robertson, 2016, Sanglerat, 2012]. Table 6 shows the average soil types in the respective geographic regions for Experiments 2, 3, and 4.

The target soil from our previous works is relatively permissive when compared to the native soils in the three geographic locations where we conducted field trials [Plowcha et al., 2018, Sun et al., 2018]. In our outdoor test range at the University of Nebraska, we find that clay is the predominant component of the soil after the first 25 to 30 mm. Due to the higher clay content, moisture content is also higher as is the compressive strength (approximate 0.6 MPa). In the mountainous terrain of Alamogordo, New Mexico, we find a higher sand content and considerably more rocks. In Nacimiento, California, a hard, dry crust with a compressive strength beyond the capabilities of our penetrometer covered the majority of the terrain. The riverbed where we conducted our field trials lacked this crust, but the underlying soil contained rocks and other impediments similar to those at White Sands.

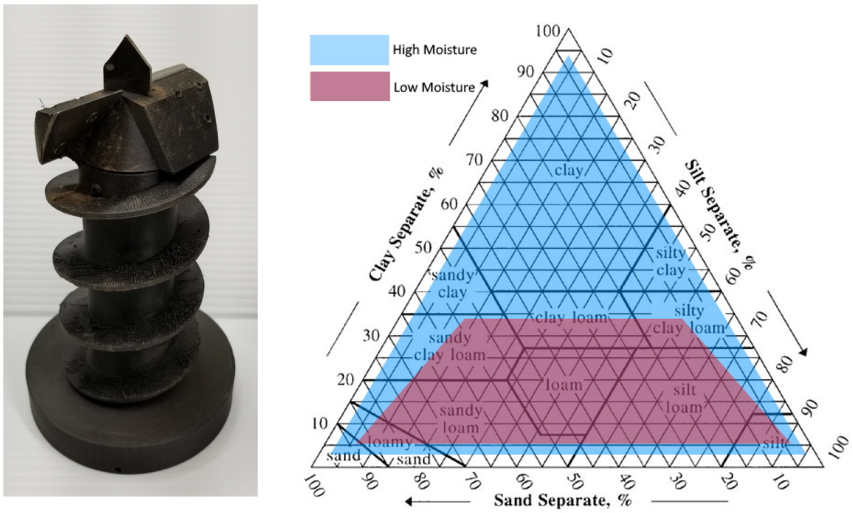

Figure 20. Spade-style bit with associated soil triangle and effectiveness overlay. The shaded moisture regions indicate where this style of bit is effective. For instance, in high-moisture clay region depicted at the top the triangle, this bit works well. However, if the clay has a low moisture content, then a different bit should be chosen

6.3.1. Weight on bit

Weight on bit is the amount of force that can be applied through the auger bit perpendicular to the material being augered. In our previous work, the digging UAS could only supply 9.8N of weight on bit for digging operations. We had a success rate of 92.5% in the prescribed target soil which was an even mix of silty clay and sand with a compressive strength of 0.4 MPa and up to 40% moisture content [Sun et al., 2018]. Our current system can supply 93.4 N of weight on bit when on level terrain. With no system malfunctions, we achieved a 100% success rate in laboratory and field trials using the originally prescribed soil type (which had to be prepared beforehand as it is not native to our geographic area).

6.3.2. Auger tip selection

We found that, by carefully selecting auger tips to match the target's general soil type, we could achieve higher sensor emplacement success rates. Spade-style auger bits have proven to be effective, general-purpose bits suited to a wide range of soil types, with the exception of dry clay. For the latter soil, the "hole-cutting" type of bit is most effective. Figures 20 and 21 show these bits with their associated U.S. Department of Agriculture soil triangles. We add color overlays to the triangles that represent the bit's effective soil types based on moisture content.

6.3.3. Analysis

We conducted a total of 27 digging trials: four at White Sands Missile Range, 13 at Camp Roberts Army National Guard base, and 10 at our outdoor test facility at the University of Nebraska. We consider a digging operation successful if the auger drills to a depth of 150 mm (see Figure 22). Between the three geographic areas previously mentioned, we conducted a total of 27 digging trials with our system in challenging soil conditions, with with 16 successful sensor installations, thus resulting in an overall success rate of 59.2%. Table 7 shows the details of these trials.

6.4. Results summary

Table 8 shows the results of the subsystems of SEEDS as totaled over the respective experiments. Again, we note that logistical constraints involving the availability of the transporting aircraft

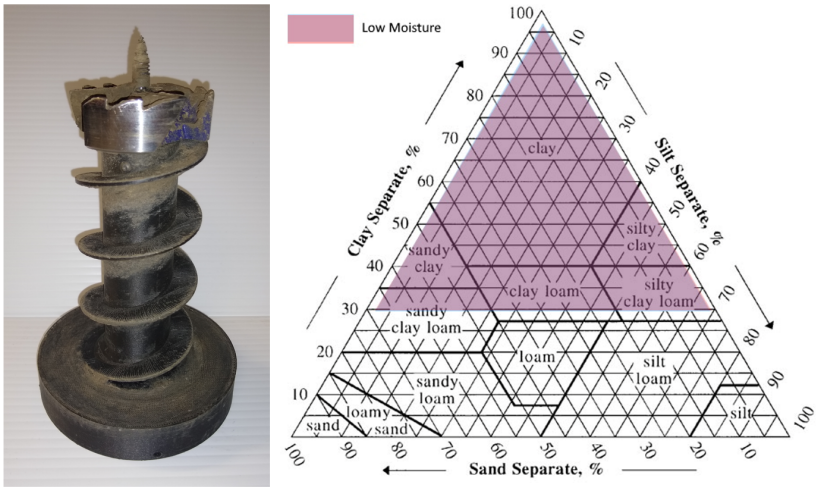

Figure 21. Hole cutting-style bit with associated soil triangle and effectiveness overlay The shaded moisture regions indicate where this style of bit is effective. For instance, this bit works well in low-moisture clay, but is less effective in most types of loam

Table 7. Digging trials analysis

Experiment #:	**2**	**3**	**4**	**TOTAL**
# of Trials	4	10	13	27
# of Successes	2	7	7	16
# of Failures	2	3	6	11
% of Successes	50	70	53.8	59.2

Experiment 2 = Alamogordo, New Mexico
Experiment 3 = Lincoln, Nebraska
Experiment 4 = Nacimiento, California

Figure 22. Successfully emplaced sensor

combined with legal considerations regarding available airspace prevented a true end-to-end test of the system.

7. Conclusion and future work

We have successfully demonstrated the ability to place subsurface ground sensors, autonomously and at distances up to 25 km from a launch point. SEEDS can be carried on a tether inside a

Table 8. Subsystems success summary

Subsystem	Experiments	Success Rate
Airborne Deployment	1,2	80.0%
Landing Zone Selection and Verification	3,4	89.8%
Autonomous Sensor Emplacement	2,3,4	59.2%

container by a larger aircraft, dropped in the vicinity of the desired sensor insertion location by parachute, autonomously jettison the container, release itself from the parachute, fly to a desired digging location, evaluate the landing area, land, implant a sensor into the ground, release it, and successfully fly away to a terminal location where the aircraft could be recovered at a later time if desired.

While we realized an 80% success rate for deploying our system from another aircraft, this round of trials could only focus on sling-load deployments, due to the limitations of the Schiebel S-100 transporting aircraft. In the future, we intend to further refine our system's freefall deployment capability. Additionally, we are actively seeking methods of operating successfully in more varied and challenging soil types. Auger design and autonomous recognition of soil type can enable more intelligent digging-control techniques and yield higher sensor-installation success rates. For our landing-zone analysis, we are considering the use of newer LiDAR systems, such as the Velodyne VLP 16, and the Intel D4XX-series of depth cameras. Finally, adapting our system to a vertical-takeoff-and-landing (VToL), fixed wing aircraft would enable in-ground sensor implantation at significantly greater distances without parachuting into the desired area.

Appendix A - System Video

A video showcasing the system described in this work can be found in the digital appendix or at https://youtu.be/c89szxtmCT4.

Appendix B - Pin-Pull Mechanism Design Issues

All of Experiment 1 and the first trial of Experiment 2 used the two pin-pull release mechanism which resulted in two failures to release from the tow frame (see Figure 24). Understanding the relationship between the aerodynamic performance of the capsule and its effect on the release mechanism was critical in minimizing future failures. In flight, the drag on the capsule would displace the capsule from a vertical orientation. This resulted in failure to release due additional force being applied perpendicular to the pin-pull mechanism which could not be overcome by the servo. Since the aircraft is rigidly attached to the capsule, we can calculate the capsule's inclination using the flight controller's logged pitch and roll values and Equation 1

$$\iota = \cos^{-1}(\cos(\phi)\ \cos(\theta)) \tag{1}$$

where ι is the angle of the capsule in reference to the perpendicular, ϕ is the capsule pitch angle, and θ is the capsule roll angle.

As the Schiebel S-100 flies a profile that attempts to maintain a constant ground speed (and we did not have access to its internal airspeed estimation) we must estimate the airspeed of our capsule based on its known course and speed over the ground and the recorded prevailing wind conditions in the area at the time of our flight [Weather Underground History and Data Archive, 2019] using Equation 2

$$S_a = S_g + (S_w\ \cos(|D_w - C_g|)) \tag{2}$$

where S_a is the airspeed of the capsule, S_g is its ground speed, S_w is the wind speed, D_w is the direction the wind is coming from, and C_g is the course the capsule is traveling over the ground.

Looking at the data from all 11 trials, we gain an understanding of the effects of airspeed on the inclination of our capsule. Even though our data is noisy, a general trend is visible. Looking at the graph in Figure 23, we see that capsule incline remains relatively vertical until 13 m/s. At this

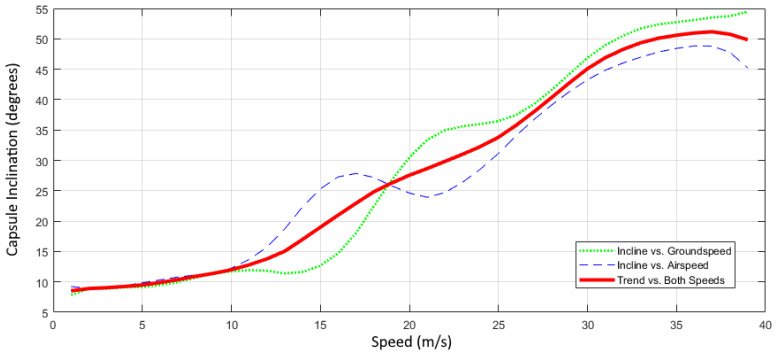

Figure 23. Effects of speed on capsule inclination - higher speeds increase the capsule's angular displacement from vertical

=

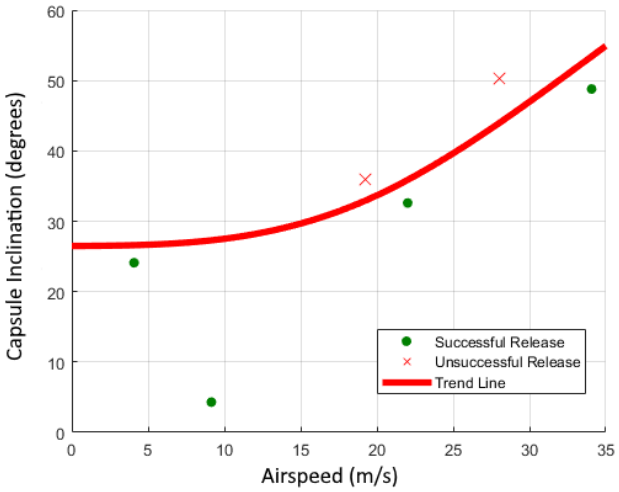

Figure 24. Capsule inclination and airspeed effects on two-point release mechanism - failures are above the red trend line

point, the drag force pushing against the capsule body increases enough to overcome the weight of the capsule and cause the inclination to increase linearly as the speed increases until the capsule's inclination has reached approximately 47°. After 47°, incline increases more slowly with speed as the cross-sectional area of the capsule begins to decrease with the majority of the lid now in the wind line.

This high angle of inclination affected our two-point release system. The additional force applied to the lid from the air stream increased the amount of torque the servo had to generate in order to pull the pins from the retention rings on the tow frame. Figure 25 shows the resultant torques based for various angles at an airspeed of 28.3 m/s. Laboratory analysis of the model of servo used in either of our pin-pull mechanisms showed that the servos could pull the pins 100% of the time as long as they only had to generate 43.3 Nm of torque. Beyond that, successful pin-pull release became increasingly intermittent until reaching a requirement of 68 Nm when failure to release was total. This degradation of servo capability explains the successful release at 36 m/s with 47° of incline and the unsuccessful release at 31.5 m/s with 52° of incline.

One trial in the initial six, however, also failed to release even though it was within wind and inclination limits. Since the container could spin freely at the end of the tether, a situation could

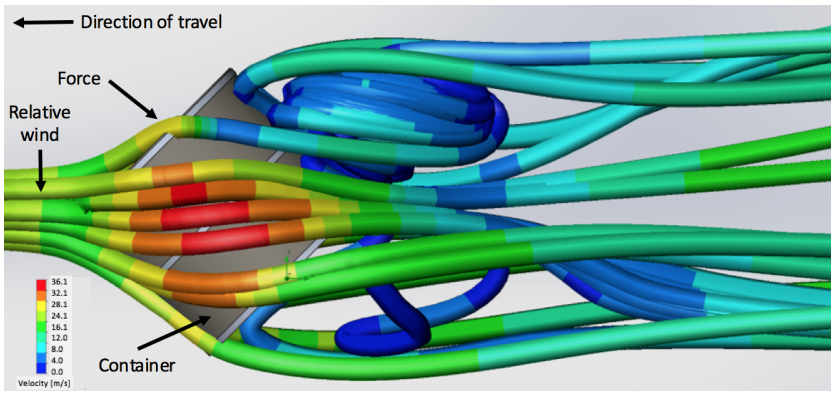

28.3 m/s

Angular Deflection	Torque on Pin-Pull
0°	27.1 N m
15°	35.3 N m
30°	40.7 N m
45°	43.3 N m

Figure 25. Angular deflection vs. torque on container release mechanism at 28.3 m/s

occur where the pin-pull mechanisms would be aligned vertically, one over the other. The uneven force applied to the lid from the relative wind could cause the lower pin-pull mechanism to become wedged in the ring of the tow frame. After the container failed to release during trial 6, we manually jettisoned the outer shell, opened the motor arms, and separated the UAS from the lid, which remained attached to the tow frame.

After the initial trial in Experiment 2, we re-designed the lid to use only one pin-pull mechanism (as shown in Figure 15b). We also imposed airspeed limits on the transporting aircraft so that releases would only be attempted with relative winds less than 25.0 m/s to the maximum extent practical. Subsequently, with the use of the one pin mechanism, the remainder of the trials in Experiment 2 successfully released from the tow frame.

Acknowledgments

This material is based upon work supported by US Strategic Command through the 55th Contracting Squadron under Contract No. FA4600-12-D-9000 and was also funded, in part, by NSF IIS-1925368 and USDA-NIFA 2017-67021-25924.

ORCID

Adam Plowcha https://orcid.org/0000-0002-0629-5319
Justin Bradley https://orcid.org/0000-0002-4201-6903
Thomas Ammon https://orcid.org/0000-0003-0866-084X
Mark Nail https://orcid.org/0000-0002-5675-0332
Brittany Duncan https://orcid.org/0000-0002-7289-8273
Carrick Detweiler https://orcid.org/0000-0002-6369-4009

References

AeroEnvironment RQ-11 Raven (2019). Retrieved Nov. 18, 2019, from https://www.avinc.com/uas/view/raven.

Anthony, D., Basha, E., Ostdiek, J., Ore, J.-P., and Detweiler, C. (2015). Surface classification for sensor deployment from uav landings. In *2015 IEEE International Conference on Robotics and Automation (ICRA)*, pages 3464–3470. IEEE.

Bishop, S. M., Curtis, K., and Sobande, B. (2010). Air-launched expendable small unmanned aircraft systems: Increasing power and extending endurance to meet operational needs. Technical report, SAE Technical Paper.

Bradley, A. C., Palo, S., LoDolce, G., Weibel, D., and Lawrence, D. (2015). Air-deployed microbuoy measurement of temperatures in the marginal ice zone upper ocean during the mizopex campaign. *Journal of Atmospheric and Oceanic Technology*, 32(5):1058–1070.

Brungardt, J. (2012). Introduction to unmanned aircraft systems. *UNMANNED AIRCRAFT SYSTEMS*, page 17.

Corke, P., Hrabar, S., Peterson, R., Rus, D., Saripalli, S., and Sukhatme, G. (2004). Autonomous deployment and repair of a sensor network using an unmanned aerial vehicle. In *IEEE International Conference on Robotics and Automation, 2004. Proceedings. ICRA'04. 2004*, volume 4, pages 3602–3608. IEEE.

Corke, P., Hrabar, S., Peterson, R., Rus, D., Saripalli, S., and Sukhatme, G. (2006). Deployment and connectivity repair of a sensor net with a flying robot. In *Experimental robotics IX*, pages 333–343. Springer.

DJI (2019). Retrieved Sept. 18, 2019, from https://www.dji.com.

Eubank, R., Atkins, E., and Meadows, G. (2010). Unattended operation of an autonomous seaplane for persistent surface and airborne ocean monitoring. In *OCEANS 2010 MTS/IEEE SEATTLE*, pages 1–8. IEEE.

Foxtech (2019). Retrieved Sept. 18, 2019, from https://foxtechfpv.com/.

Fujishima, M., Nishiura, I., Kakino, Y., and Matsubara, A. (2000). Integration of adaptive control functions for drilling in intelligent machine tools. In *Proceedings of the Sixth International Conference on Automation Technology*, volume 1, pages 531–535.

Henderson, L., Glaser, T., and Kuester, F. (2017). Towards bio-inspired structural design of a 3d printable, ballistically deployable, multi-rotor uav. In *2017 IEEE Aerospace Conference*, pages 1–7. IEEE.

Insitu ScanEagle (2020). Retrieved Feb. 11, 202, from https://www.insitu.com/information-delivery/unmanned-systems/scaneagle.

Islam, A., Houston, A. L., Shankar, A., and Detweiler, C. (2019). Design and evaluation of sensor housing for boundary layer profiling using multirotors. *Sensors*, 19(11):2481.

Jo, S., Lee, B., Oh, J., Song, J., Lee, C., Kim, S., and Suk, J. (2019). Experimental study of in-flight deployment of a multicopter from a fixed-wing uav. *International Journal of Aeronautical and Space Sciences*, pages 1–13.

Johnson, A. and Ivanov, T. (2011). Analysis and testing of a lidar-based approach to terrain relative navigation for precise lunar landing. In *AIAA Guidance, Navigation, and Control Conference*, page 6578.

Kendoul, F. (2012). Survey of advances in guidance, navigation, and control of unmanned rotorcraft systems. *Journal of Field Robotics*, 29(2):315–378.

Klinkmueller, K., Wieck, A., Holt, J., Valentine, A., Bluman, J. E., Kopeikin, A., and Prosser, E. (2019). Airborne delivery of unmanned aerial vehicles via joint precision airdrop systems. In *AIAA Scitech 2019 Forum*, page 2285.

Kong, W., Zhou, D., Zhang, D., and Zhang, J. (2014). Vision-based autonomous landing system for unmanned aerial vehicle: A survey. In *2014 international conference on multisensor fusion and information integration for intelligent systems (MFI)*, pages 1–8. IEEE.

Lacerda, M. G., Paulino, A. D. C., Shiguemori, E. H., Damiao, A. J., Guimaraes, L. N. F., and dos Anjos, C. S. (2018). Identification and classification of drop zones and helicopter landing zones in images obtained by small size remotely piloted aircraft systems. In *IGARSS 2018-2018 IEEE International Geoscience and Remote Sensing Symposium*, pages 7906–7909. IEEE.

Lobik, D. (1998). Helicopter dynamic rollover. *Naval Postgraduate School, Monterey, CA*, 20.

Lussier, M. E., Bradley, J. M., and Detweiler, C. (2019). Extending endurance of multicopters: The current state-of-the-art. In *AIAA Scitech 2019 Forum*, page 1790.

Meadows, G., Atkins, E., Washabaugh, P., Meadows, L., Bernal, L., Gilchrist, B., Smith, D., VanSumeren, H., Macy, D., Eubank, R., et al. (2009). The flying fish persistent ocean surveillance platform. In *AIAA Infotech@ Aerospace Conference and AIAA Unmanned... Unlimited Conference*, page 1902.

Mellinger, J. C., Burak Ozdoganlar, O., DeVor, R. E., and Kapoor, S. G. (2002). Modeling chip-evacuation forces and prediction of chip-clogging in drilling. *J. Manuf. Sci. Eng.*, 124(3):605–614.

Natividade, J., Prado, J., and Marques, L. (2017). Low-cost multi-spectral vegetation classification using an unmanned aerial vehicle. In *2017 IEEE International Conference on Autonomous Robot Systems and Competitions (ICARSC)*, pages 336–342. IEEE.

Nie, S., Wang, C., Dong, P., Xi, X., Luo, S., and Qin, H. (2017). A revised progressive tin densification for filtering airborne lidar data. *Measurement*, 104:70–77.

Northrop Grumman Firescout (2020). Retrieved Feb. 11, 202, from https://www.northropgrumman.com/air/fire-scout/.

Ore, J.-P. and Detweiler, C. (2018). Sensing water properties at precise depths from the air. *Journal of Field Robotics*, 35(8):1205–1221.

Parness, A., Frost, M., Thatte, N., and King, J. P. (2012). Gravity-independent mobility and drilling on natural rock using microspines. In *2012 IEEE International Conference on Robotics and Automation*, pages 3437–3442. IEEE.

Pister, K. S. (2001). Tracking vehicles with a uav-delivered sensor network.

Planck Aerosystems (2019). Retrieved Feb. 11, 202, from https://www.planckaero.com/truckdrone.

Plowcha, A., Sun, Y., Detweiler, C., and Bradley, J. (2018). Predicting digging success for unmanned aircraft system sensor emplacement. In *Proceeding of the 2018 International Conference on Experimental Robotics (ISER 2018)*, Buenos Aires, Argentina.

Robertson, P. (2016). Cone penetration test (cpt)-based soil behaviour type (sbt) classification system—an update. *Canadian Geotechnical Journal*, 53(12):1910–1927.

Sanglerat, G. (2012). *The penetrometer and soil exploration*. Elsevier.

Scherer, S., Chamberlain, L., and Singh, S. (2012). Autonomous landing at unprepared sites by a full-scale helicopter. *Robotics and Autonomous Systems*, 60(12):1545–1562.

Schwarzbach, M., Kondak, K., Laiacker, M., Shih, C.-Y., and Marrón, P. J. (2012). Helicopter uav systems for in situ measurements and sensor placement. In *2012 IEEE International Geoscience and Remote Sensing Symposium*, pages 4766–4769. IEEE.

Shi, X., Deng, Z., Quan, Q., Tang, D., Hou, X., and Jiang, S. (2014). Development of a drilling and coring test-bed for lunar subsurface exploration and preliminary experiments. *Chinese Journal of Mechanical Engineering*, 27(4):673–682.

Singh, S., Cover, H., Stambler, A., Grocholsky, B., Mishler, J., Hamner, B., Strabala, K., Sherwin, G., Kaess, M., Hemann, G., et al. (2016). Perception for safe autonomous helicopter flight and landing. In *American Helicopter Society 72nd Annual Forum, West Palm Beach, Florida, USA*.

Stewart, R., Chang, L., Sudarshan, S., Becker, A., and Huang, L. (2016). An unmanned aerial vehicle with vibration sensing ability (seismic drone). In *SEG Technical Program Expanded Abstracts 2016*, pages 225–229. Society of Exploration Geophysicists.

Sun, Y., Plowcha, A., Nail, M., Elbaum, S., Terry, B., and Detweiler, C. (2018). Unmanned aerial auger for underground sensor installation. In *2018 IEEE/RSJ International Conference on Intelligent Robots and Systems (IROS)*, pages 1374–1381. IEEE.

Weather Underground History and Data Archive (2019). Retrieved June 28, 2019, from https://www.wunderground.com/history/.

Whalley, M., Takahashi, M., Tsenkov, P., Schulein, G., and Goerzen, C. (2009). Field-testing of a helicopter uav obstacle field navigation and landing system. In *65th Annual Forum of the American Helicopter Society, Grapevine, TX*.

Zacny, K. and Cooper, G. (2006). Considerations, constraints and strategies for drilling on mars. *Planetary and Space Science*, 54(4):345–356.

Zacny, K., Wilson, J., Chu, P., and Craft, J. (2011). Prototype rotary percussive drill for the mars sample return mission. In *2011 Aerospace Conference*, pages 1–8. IEEE.

How to cite this article: Plowcha, A., Bradley, J., Hogberg, J., Ammon, T., Nail, M., Duncan, B., & Detweiler, C. (2022). Autonomous, long-range, sensor emplacement using unmanned aircraft systems. *Field Robotics, 2*, 437–467.